

# MODELING THE DETECTION CAPABILITY OF HIGH-SPEED SPIKING CAMERAS

*Junwei Zhao<sup>1</sup>, Zhaofei Yu<sup>1,\*</sup>, Lei Ma<sup>1,2,\*</sup>, Ziluo Ding<sup>1</sup>, Shiliang Zhang<sup>1</sup>, Yonghong Tian<sup>1</sup>, Tiejun Huang<sup>1,2</sup>*

<sup>1</sup>Institute of Digital Media, Peking University, Beijing, China

<sup>2</sup>Beijing Academy of Artificial Intelligence, Beijing, China

## ABSTRACT

The novel working principle enables spiking cameras to capture high-speed moving objects. However, the applications of spiking cameras can be affected by many factors, such as brightness intensity, detectable distance, and the maximum speed of moving targets. Improper settings such as weak ambient brightness and too short object-camera distance, will lead to failure in the application of such cameras. To address the issue, this paper proposes a modeling algorithm that studies the detection capability of spiking cameras. The algorithm deduces the maximum detectable speed of spiking cameras corresponding to different scenario settings (e.g., brightness intensity, camera lens, and object-camera distance) based on the basic technical parameters of cameras (e.g., pixel size, spatial and temporal resolution). Thereby, the proper camera settings for various applications can be determined. Extensive experiments verify the effectiveness of the modeling algorithm. To our best knowledge, it is the first work to investigate the detection capability of spiking cameras.

**Index Terms**— Neuromorphic Vision Sensing, Spike Signal Processing, Emerging Multimedia Applications

## 1. INTRODUCTION

Conventional cameras work on the frame-based imaging principle, where each frame represents the accumulation of luminance over an exposure time. Constrained by a fixed exposure time, conventional cameras struggle in high-speed scenarios [1, 2, 3]. Recent years have witnessed the prosperous development of neuromorphic cameras, which are widely used in a variety of applications such as detection [4, 5], tracking [6, 7], recognition [8, 9, 10], optical flow estimation [11, 12], and reconstruction [13, 14]. According to the working principle, neuromorphic cameras can be roughly categorized as event cameras (following the differential principle) [15, 16, 17] and spiking cameras (following the integral principle) [18, 19]. In event cameras, each pixel encodes the change of luminance to asynchronous events. As a comparison, each pixel of spiking cameras keeps recording luminance and emits a spike once

This work was supported by the National Natural Science Foundation of China (62088102, 62176003, U20B2052, 61936011) and the National Key R&D Program of China (2018YFE0118400, 2021ZD0109802).

\* Corresponding author (✉: yuzf12@pku.edu.cn; lei.ma@pku.edu.cn)

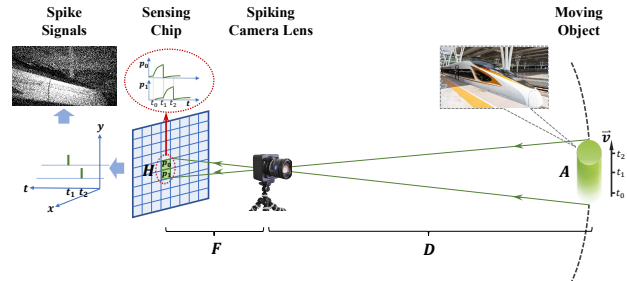


**Fig. 1.** The correlation between spike signals and scene radiance is modelled, thus can deduce the detection capability of spiking cameras under different scenarios and further provide application guidance. E.g., a high-speed train is successfully captured with the guidance of the modeling algorithm.

the accumulated intensity reaches a threshold. The distinctive imaging principle and data representation allow neuromorphic cameras to mitigate the limitations imposed by fixed exposure time, thereby increasing their temporal resolution and potential for capturing high-speed objects [20].

Existing neuromorphic cameras are implemented based on CMOS technology. The photo-electric conversion time of each pixel bounds the maximum sampling frequency of spike signals and the capability of detecting high-speed objects [21]. Improper settings including too-short detection distance, very long focal length of lens, and weak brightness, will lead to the failure in practical applications of neuromorphic cameras. For example, weak brightness degrades the real-time sampling frequency of neuromorphic cameras, introducing challenges in detecting high-speed moving objects [22]. However, manuals of neuromorphic cameras only provide basic technical parameters, such as temporal resolution, dynamic range, and supply voltage. Although those parameters can reflect the property of a camera, it is still difficult for users to get proper configurations for different application scenarios. Thus, an algorithm that guides users to determine the proper settings of neuromorphic cameras for different scenarios are appealing for investigating.

This paper proposes an early work that studies the detection capability of high-speed spiking cameras. As illustrated in Fig. 1, we derive the correlation between spike signals and scene radiance. Based on it, the applicable settings (including brightness intensity, configuration of camera lens, maximum speed of moving targets, and object-camera distance) of spiking cameras can be determined, ensuring them to work

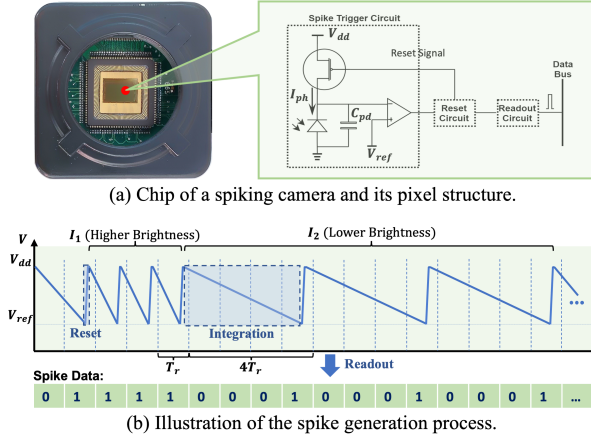


**Fig. 2.** The working principle of spiking cameras.

properly under different scenes. We build an experimental system to validate the modeling algorithm. Moreover, we also perform real-world application cases such as capturing high-speed travelling trains using a spiking camera. Extensive experiments show that, our algorithm provides effective and convenient guidance for spiking camera applications.

## 2. WORKING PRINCIPLE OF SPIKING CAMERAS

We formulate the modeling algorithm based on the spiking camera adopted in [18]. Fig. 2 (a) shows that the pixel of the spiking camera comprises three parts: spike trigger, reset and readout circuits. Fig. 2 (b) shows that the working principle of the camera contains three states: integration, reset, and readout. In the integration state, the photo-diode in each pixel converts the photo-current  $\ell_{ph}$  into the voltage on capacitance  $C_{pd}$ . As the photo-diode continues to generate electric charges, the voltage on capacitance will drop. When its value reaches the threshold  $V_{ref}$ , the comparator flips over. Once the reset circuit detects the flip signal, the pixel enters the reset state. The reset circuit then generates a 1-bit signal to reset the photo-diode. After a very short time interval, a new integration stage is resumed. Meanwhile, the 1-bit signal is stored in the readout circuit. In the readout state, the signal stored in the readout circuit is transmitted to the data bus by a readout clock (40KHz). Afterwards, the readout circuit clears its storage. According to the above analysis and Fig. 2, the condition that a pixel emits a spike can be formulated as,

$$\frac{1}{C_{pd}} \int \ell_{ph} dt \geq (V_{dd} - V_{ref}). \quad (1)$$

## 3. MODELING ALGORITHM

The modeling algorithm aims to determine whether the camera can be applied in a specific scenario or to provide proper applicable settings for an application. To this purpose, we derive the relation between the detectable speed  $v$ , brightness

intensity  $I$ , detection distance  $D$ , and focal length of lens  $F$ , as shown in Fig. 1. The derivation is divided into the three steps: 1)  $\langle I \Rightarrow f_r \rangle$  Derive the relation of  $I$  with the real-time spike firing rate  $f_r$  of spiking cameras; 2)  $\langle D \& F \Rightarrow A_{\min} \rangle$  Derive the relation among  $D$ ,  $F$ , and minimum resolvable distance  $A_{\min}$ ; 3)  $\langle I \& D \& F \Rightarrow v \rangle$  Based on the constraint of  $A_{\min}$  and  $f_r$  to  $v$ , establish the relation of  $I$ ,  $D$ , and  $F$  to  $v$ .

- $\langle I \Rightarrow f_r \rangle$  Each pixel on the sensing chip keeps recording the brightness from target scenes. In spiking cameras, a linear relation  $\lambda$  is observed between brightness intensity  $I$  and the photo-current  $\ell_{ph}$  of pixel photodiodes. According to Eq. 1, the condition that a pixel emits a spike can be formulated as,

$$\int_t^{t+\Delta t} \lambda I dt \geq C_{pd}(V_{dd} - V_{ref}), \quad (2)$$

where  $\Delta t$  is the integrating time of a pixel. As the readout of spike signals is constrained by the readout clock,  $\Delta t$  is equal to  $nT_r$ , where  $T_r = \frac{1}{40K} s = 25\mu s$ .  $T_r$  is defined as the temporal resolution of spiking cameras. According to Eq. 2, given the brightness intensity  $I$ , the minimal integrating time that is necessary for emitting a spike can be calculated as  $n = \lceil \frac{C_{pd}(V_{dd} - V_{ref})}{\lambda T_r} \rceil$ . Thus, the real-time spike firing rate  $f_r$  can be calculated as follows:

$$f_r = \frac{1}{\Delta t} = \frac{1}{nT_r} = \frac{1}{\lceil \frac{C_{pd}(V_{dd} - V_{ref})}{\lambda T_r} \rceil T_r}. \quad (3)$$

According to the above equation, lower brightness leads to the decrease on spike firing rate. As shown in Fig. 2 (b), it can be observed that, when the  $I$  changes from  $I_1$  to  $I_2$ , the  $f_r$  decreases from  $\frac{1}{T_r}$  to  $\frac{1}{4T_r}$ . Note that the maximum spike firing rate  $f_{max}$  is  $\frac{1}{T_r}$ . Therefore, based on the Eq. 2, we can derive the saturated state of brightness intensity  $I_s$  as expressed in Eq. 4. The value of  $\lambda$  can be experimentally determined as well. When the  $I$  exceeds  $I_s$ , the  $f_r$  reaches the maximum and no longer changes with the  $I$ .

$$I_s = \frac{C_{pd}(V_{dd} - V_{ref})}{\lambda T_r}. \quad (4)$$

- $\langle D \& F \Rightarrow A_{\min} \rangle$  As shown in Fig. 1, a target at distance  $D$  moves at a speed  $v$ , and projects an inverted image on the sensing chip through lens. The projected pixels keep recording the brightness independently and emit a spike once the voltage reaches a threshold. Suppose that the lengths of the target and its image are  $A$  and  $H$ , respectively, the relation between them can be represented as follows according to the law of convex lens imaging:

$$\frac{F}{H} = \frac{D}{A}. \quad (5)$$

Based on Eq. 5 and given the pixel size  $a$  of the sensor, the minimum resolvable distance  $A_{\min}$  of spiking cameras at the distance  $D = D_0$  can be calculated as,

$$A_{\min} = \frac{D_0 \cdot a}{F}. \quad (6)$$

**Table 1.** Basic technical parameters of the spiking sensor.

Parameter	Value
Array Size ( $W \times H$ )	400×250
Temporal Resolution ( $T_r$ )	25 $\mu$ s
Pixel Size ( $a \times a$ )	20 $\mu$ m×20 $\mu$ m
Supply Voltage ( $V_{dd}$ )	3V
Reference Voltage of Comparator ( $V_{ref}$ )	1V
Capacitance of Photodiode ( $C_{pd}$ )	15fF

- $\langle I \& D \& F \Rightarrow v \rangle$  As shown in Eq. 6, each pixel samples the brightness of an  $A_{min} \times A_{min}$  area (hereinafter, called the  $A^2$  area) at the distance  $D_0$  to the lens. To ensure that sufficient information is captured from a high-speed continuous motion, a pixel needs to emit at least one spike that sampled from an  $A^2$  area (i.e., the brightness of an  $A^2$  area needs at least one spike for information representation). According to Eq. 3, when the brightness intensity  $I$  is lower than  $I_s$ , the real-time spike firing rate decreases from  $\frac{1}{T_r}$  to  $\frac{1}{nT_r}$ . Hence, we can derive the upper bound of the detectable speed of targets as,

$$v \leq \frac{A_{min}}{nT_r} = \frac{A_{min}}{\lceil \xi I^{-1} \rceil T_r}, \quad (\text{let } \xi = \frac{C_{pd}(V_{dd} - V_{ref})}{\lambda T_r}). \quad (7)$$

Combining Eq. 6 with Eq. 7, the detectable speed of moving targets can be formulated as,

$$v \leq \frac{aD}{F \lceil \xi I^{-1} \rceil T_r}, \quad (8)$$

where  $a$  and  $T_r$  are the basic technical parameters referred from Tab. 1,  $F$  is related to the lens of spiking cameras,  $I$  and  $D$  are related to application scenes. In this way, the applicable settings of spiking cameras can be determined.

#### 4. EXPERIMENTS

- **Validation Experiments:** We conduct two group of experiments, i.e., rotation and translation experiment, to verify the proposed modeling algorithm. The spiking camera adopted in experiments is shown in Fig. 3 (a). This camera has the temporal resolution of 50 $\mu$ s, and the other technical parameters are same as Tab. 1. The rotation experiment aims to verify the modeling result through rotation motion, and we build an experimental system (Fig. 3 (b)) where the applicable settings can be manually configured. For instance, the brightness intensity can be adjusted by curtains, the rotating speed of fan blades can be modulated by the speed controller, and the object-camera distance can be measured precisely by the ruler. In rotation experiments, we set six different experimental configurations (e.g.,  $D$ ,  $I$ , and  $F = 8mm$ ), as recorded in Tab. 2. According to the technical parameters and experimental configurations, the maximum detectable speed (denoted as  $V_m$ ) in each set of experiment can be calculated by Eq. 8. As a contrast, we set the rotating speed of fan blades as  $V_m$  and  $(1.2 \times \sim 1.5 \times) V_m$ , respectively. Afterwards, we use the spiking camera to record high-speed rotating motions. Given that

**Table 2.** The configuration of rotation experiments (Fig. 3 (c)), and the evaluation results of the reconstructed images by TFI corresponding to each set of experiment.

No.	$D(m)$	Experimental Configurations		Evaluation Results	
		$I(\text{lx})$	$v(\text{m/s})$	TDE↑	BIBQ↓
1-1	0.5	2000	4.2 ( $V_m$ )	<b>10.03</b>	<b>63.78</b>
1-2			6.3 (1.5 $V_m$ )	9.72	69.73
2-1		6000	8.3 ( $V_m$ )	<b>9.65</b>	<b>29.36</b>
2-2			11.6 (1.4 $V_m$ )	9.43	32.33
3-1		12000	25 ( $V_m$ )	<b>9.34</b>	<b>12.59</b>
3-2			30 (1.2 $V_m$ )	9.07	16.48
4-1	1.0	2000	8.3 ( $V_m$ )	<b>10.19</b>	<b>60.74</b>
4-2			12.5 (1.5 $V_m$ )	9.82	65.29
5-1		6000	25 ( $V_m$ )	<b>9.71</b>	<b>18.12</b>
5-2			32.5 (1.3 $V_m$ )	9.52	22.54
6-1		12000	50 ( $V_m$ )	<b>11.12</b>	<b>14.79</b>
6-2			60 (1.2 $V_m$ )	10.62	20.62

the camera captures sufficient information about the moving targets with the speed  $v \leq V_m$ , the spike-based algorithms can reconstruct images from raw data. If the moving speed exceeds  $V_m$ , the reconstructed images will suffer from information loss (e.g., motion blur) as shown in Fig. 3 (c). Note that the rotating radius of the fan (denoted as  $R$ ) is 15 cm, and rotating speed (denoted as  $V_{rot}$  rps (round per second)) can be manually set. Then, the speed of chars on fan blades can be calculated as:  $v = 2\pi R V_{rot}/60$ .

In the translation experiment, we perform real-world cases. Specifically, we use the spiking camera to record a train (type CR400BF) passing through the platform on main-line at a high speed (350 km/h). Before the experiment, to ensure that the spiking camera can record the high-speed motion, precise applicable settings should be determined. The experiment is conducted on a sunny noon (bright intensity is saturated), thereby ensuring that spiking camera can work at the maximum spike firing rate. Given that the  $v$  of the train is 350 km/h, and the  $F$  of lens is 16 mm, the distance between the train and lens should be set to at least 3.9 m according to Eq. 8. Based on above calculation results, we position the spiking camera on the platform approximately 4 m away from the train. The camera is turned on to record data while the train is passing through. We also capture high-speed cars adopting the similar procedure. The spike data and the corresponding reconstructed images are shown in Fig. 3(d).

- **Experimental Results:** We adopt the Texture From Inter-spike-interval (TFI) method [19] to reconstruct images from raw spikes. This method only takes the inter-spike interval to reconstruct gray-scale images, and does not introduce any optimal techniques and referenced information. Thus, the quality of the images reconstructed by TFI can reflect the information carried by raw spikes. To quantitatively evaluate the reconstructed images, we employ the Two-Dimensional Entropy (TDE) [23] and Blind Image Quality Index (BIQI) [24] for metrics. The larger indicator of TDE represents better, while contrary for BIQI. The evaluation results summarized in Tab. 2 show that, the images reconstructed from

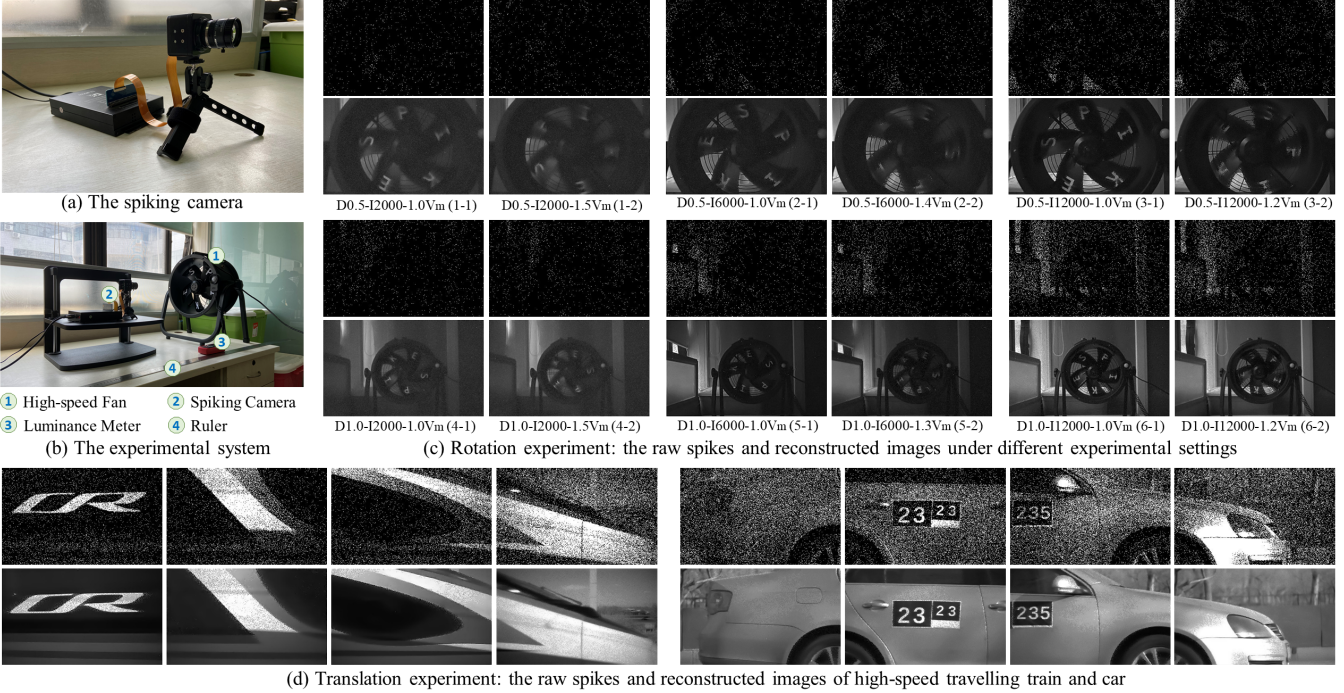


**Fig. 3.** Rotation and translation experiments verify the modeling algorithm. We build an experimental system to perform rotation experiments, and record high-speed travelling train and car under the guidance of the calculated applicable settings.

the scenes with  $v = V_m$  have better quality than those from the scenes with  $v > V_m$ . Fig. 3 (c) shows that, the reconstructed images of chars in the scenes with  $v > V_m$  are severely blurred. In addition, Fig. 3 (d) shows that, the high-speed train and car are successfully recorded under the guidance of the calculated applicable settings. Above experiments demonstrate that the modeling algorithm is effective for both rotation and translation motions. Given that the motion within the imaging plane of spiking cameras can be decomposed into translation and rotation, we hence conclude that the proposed method is valid for different motion scenarios.

• **Applications:** Exploiting the modeling algorithm, we can determine whether the camera can work properly in a specific case. In turn, given an application scenario, we can utilize this algorithm to get applicable settings for the camera to work properly. Furthermore, we elaborate three scenarios (with different brightness intensity, camera lens, and distance) and calculate the corresponding maximum detectable speed of moving targets, as recorded in Tab. 3. The first scenario is the sunny noonday with sufficient sunshine that brightness intensity exceeds the saturated state  $I_s$  (12000 lx). Tab. 3 (a) shows that, spiking cameras have a strong capability of detecting high-speed moving objects, and thus can be applied to aeroplanes or trains. The second scenario is the under-saturated condition of brightness, such as morning or cloudy weather. Tab. 3 (b) shows that, the upper bound of maximum detectable speed decreases, but the camera still remains the capability of detecting moving cars or motorbikes, thus can be used in autonomous driving. Tab. 3 (c) indicates that, the high-speed detecting capability decreases a lot in dark light conditions such as nightfall.

**Table 3.** The detection capability of the spiking camera [18] for high-speed moving objects under different scenarios.

(a) Brightness condition of saturated state

Brightness ( $I/1x$ )	Focal Length ( $F/mm$ )	Object-Camera Distance ( $D/m$ )			
		$D_1=1$	$D_2=10$	$D_3=20$	$D_4=30$
$I \geq 12000$ ( $n = 1$ )	$F = 50$	16 m/s	160 m/s	320 m/s	480 m/s
	$F = 25$	32 m/s	320 m/s	640 m/s	960 m/s
	$F = 16$	50 m/s	500 m/s	1000 m/s	1500 m/s

(b) Brightness condition of under-saturation

Brightness ( $I/1x$ )	Focal Length ( $F/mm$ )	Object-Camera Distance ( $D/m$ )			
		$D_1=1$	$D_2=15$	$D_3=25$	$D_4=50$
$I = 6000$ ( $n = 2$ )	$F = 50$	8 m/s	120 m/s	200 m/s	400 m/s
	$F = 25$	16 m/s	240 m/s	400 m/s	800 m/s
	$F = 16$	25 m/s	375 m/s	625 m/s	1250 m/s

(c) Brightness condition of dark

Brightness ( $I/1x$ )	Focal Length ( $F/mm$ )	Object-Camera Distance ( $D/m$ )			
		$D_1=1$	$D_2=5$	$D_3=10$	$D_4=15$
$I = 2000$ ( $n = 6$ )	$F = 50$	2.6 m/s	13.3 m/s	26.6 m/s	40 m/s
	$F = 25$	5.3 m/s	26.6 m/s	53.3 m/s	80 m/s
	$F = 16$	8.3 m/s	41.6 m/s	83.3 m/s	125 m/s

\* The speeds recorded in the tables represent the maximum detectable speed under the conditions with  $I$ ,  $D$ , and  $F$ .

## 5. CONCLUSION

The bio-inspired sensing principle enables neuromorphic cameras advantageous in high-speed applications. In recent years, such cameras have been widely used in drones, robots, autonomous cars, etc. However, there are few attempts trying to investigate the detection capability of spiking cameras for high-speed targets. We analyze the correlation between spike signals and scene radiance, and put forward the modeling algorithm. We believe that the proposed straightforward approach has the potential to ignite more efforts on neuromorphic cameras, as well as broader applications.

## 6. REFERENCES

- [1] Henri Rebucq, René Ranftl, Vladlen Koltun, and Davide Scaramuzza, “High speed and high dynamic range video with an event camera,” *IEEE transactions on pattern analysis and machine intelligence*, vol. 43, no. 6, pp. 1964–1980, 2019.
- [2] Guillermo Gallego, Tobi Delbruck, Garrick Michael Orchard, Chiara Bartolozzi, Brian Taba, Andrea Censi, Stefan Leutenegger, Andrew Davison, Jorg Conradt, Kostas Daniilidis, et al., “Event-based vision: A survey,” *IEEE transactions on pattern analysis and machine intelligence*, vol. 44, no. 1, pp. 154–180, 2020.
- [3] Tiejun Huang, Yajing Zheng, Zhaofei Yu, Rui Chen, Yuan Li, Ruiqin Xiong, Lei Ma, Junwei Zhao, Siwei Dong, Lin Zhu, et al., “1000x faster camera and machine vision with ordinary devices,” *arXiv preprint arXiv:2201.09302*, 2022.
- [4] Jacques Manderscheid, Amos Sironi, Nicolas Bourdis, Davide Migliore, and Vincent Lepetit, “Speed invariant time surface for learning to detect corner points with event-based cameras,” in *Proceedings of the IEEE/CVF Conference on Computer Vision and Pattern Recognition*, 2019, pp. 10245–10254.
- [5] Xi Peng, Bo Zhao, Rui Yan, Huajin Tang, and Zhang Yi, “Bag of events: An efficient probability-based feature extraction method for aer image sensors,” *IEEE transactions on neural networks and learning systems*, vol. 28, no. 4, pp. 791–803, 2016.
- [6] Lan Xu, Weipeng Xu, Vladislav Golyanik, Marc Habermann, Lu Fang, and Christian Theobalt, “Eventcap: Monocular 3d capture of high-speed human motions using an event camera,” in *Proceedings of the IEEE/CVF Conference on Computer Vision and Pattern Recognition*, 2020, pp. 4968–4978.
- [7] Daniel Gehrig, Henri Rebucq, Guillermo Gallego, and Davide Scaramuzza, “Eklt: Asynchronous photometric feature tracking using events and frames,” *International Journal of Computer Vision*, vol. 128, no. 3, pp. 601–618, 2020.
- [8] Aaron Chadha, Yin Bi, Alhabib Abbas, and Yiannis Andreopoulos, “Neuromorphic vision sensing for cnn-based action recognition,” in *ICASSP 2019-2019 IEEE International Conference on Acoustics, Speech and Signal Processing*. IEEE, 2019, pp. 7968–7972.
- [9] Jinjian Wu, Chuanwei Ma, Xiaojie Yu, and Guangming Shi, “Denoising of event-based sensors with spatial-temporal correlation,” in *ICASSP 2020-2020 IEEE International Conference on Acoustics, Speech and Signal Processing*. IEEE, 2020, pp. 4437–4441.
- [10] Shane Harrigan, Sonya Coleman, Dermot Kerr, Pratheepan Yoganathan, Zheng Fang, and Chengdong Wu, “Neural coding strategies for event-based vision data,” in *ICASSP 2020-2020 IEEE International Conference on Acoustics, Speech and Signal Processing*. IEEE, 2020, pp. 2468–2472.
- [11] Federico Paredes-Vallés, Kirk YW Scheper, and Guido CHE de Croon, “Unsupervised learning of a hierarchical spiking neural network for optical flow estimation: From events to global motion perception,” *IEEE transactions on pattern analysis and machine intelligence*, vol. 42, no. 8, pp. 2051–2064, 2019.
- [12] Mohammed Almatrafi, Raymond Baldwin, Kiyoharu Aizawa, and Keigo Hirakawa, “Distance surface for event-based optical flow,” *IEEE transactions on pattern analysis and machine intelligence*, vol. 42, no. 7, pp. 1547–1556, 2020.
- [13] Liyuan Pan, Cedric Scheerlinck, Xin Yu, Richard Hartley, Miaomiao Liu, and Yuchao Dai, “Bringing a blurry frame alive at high frame-rate with an event camera,” in *Proceedings of the IEEE/CVF Conference on Computer Vision and Pattern Recognition*, 2019, pp. 6820–6829.
- [14] Lin Wang, Tae-Kyun Kim, and Kuk-Jin Yoon, “Eventsr: From asynchronous events to image reconstruction, restoration, and super-resolution via end-to-end adversarial learning,” in *Proceedings of the IEEE/CVF Conference on Computer Vision and Pattern Recognition*, 2020, pp. 8315–8325.
- [15] Christoph Posch, Daniel Matolin, and Rainer Wohlgenannt, “An asynchronous time-based image sensor,” in *2008 IEEE International Symposium on Circuits and Systems*, 2008, pp. 2130–2133.
- [16] Tobi Delbrück, Bernabe Linares-Barranco, Eugenio Culurciello, and Christoph Posch, “Activity-driven, event-based vision sensors,” in *Proceedings of 2010 IEEE International Symposium on Circuits and Systems*. IEEE, 2010, pp. 2426–2429.
- [17] Shoushun Chen and Menghan Guo, “Live demonstration: Celex-v: a 1m pixel multi-mode event-based sensor,” in *2019 IEEE/CVF Conference on Computer Vision and Pattern Recognition Workshops*. IEEE, 2019, pp. 1682–1683.
- [18] Jin Han, Chu Zhou, Peiqi Duan, Yehui Tang, Chang Xu, Chao Xu, Tiejun Huang, and Boxin Shi, “Neuromorphic camera guided high dynamic range imaging,” in *Proceedings of the IEEE/CVF Conference on Computer Vision and Pattern Recognition*, 2020, pp. 1730–1739.
- [19] Lin Zhu, Siwei Dong, Jianing Li, Tiejun Huang, and Yonghong Tian, “Retina-like visual image reconstruction via spiking neural model,” in *Proceedings of the IEEE/CVF Conference on Computer Vision and Pattern Recognition*, 2020, pp. 1438–1446.
- [20] Annamalai Lakshmi, Anirban Chakraborty, and Chetan S Thakur, “Neuromorphic vision: From sensors to event-based algorithms,” *Wiley Interdisciplinary Reviews: Data Mining and Knowledge Discovery*, vol. 9, no. 4, pp. e1310, 2019.
- [21] Munir El-Desouki, M Jamal Deen, Qiyin Fang, Louis Liu, Frances Tse, and David Armstrong, “Cmos image sensors for high speed applications,” *Sensors*, vol. 9, no. 1, pp. 430–444, 2009.
- [22] Jing Gao, Yanzhao Wang, Kaiming Nie, Zhiyuan Gao, and Jiangtao Xu, “The analysis and suppressing of non-uniformity in a high-speed spike-based image sensor,” *Sensors*, vol. 18, no. 12, pp. 4232, 2018.
- [23] Li Xi, Liu Guosui, and Jinlin Ni, “Autofocusing of isar images based on entropy minimization,” *IEEE Transactions on Aerospace and Electronic Systems*, vol. 35, no. 4, pp. 1240–1252, 1999.
- [24] AK Moorthy and AC Bovik, “A modular framework for constructing blind universal quality indices,” *IEEE Signal Processing Letters*, vol. 17, pp. 7, 2009.